Supplementary material

Timescales of dynamic stall development on a vertical-axis wind turbine blade

Sébastien Le Fouest, Daniel Fernex, and Karen Mulleners*

Institute of Mechanical Engineering, École Polytechnique Fédérale de Lausanne (EPFL), CH-1015 Lausanne, Switzerland

*Corresponding author. E-mail:karen.mulleners@epfl.ch

1. Vertical-axis wind turbine model

A scaled-down model of a single-bladed H-type Darrieus wind turbine was mounted in the centre of the test section. The turbine has variable diameter D that was kept constant here at 30 cm. Up to three blades can be attached to the rotor arms through straight shafts that are held from the top. Here, we used the single-blade configuration to focus on the flow development around the blade in the absence of interference from the wakes of other blades. The turbine blade itself was 3D printed using a photosensitive polymer resin (Formlabs Form 2 stereolithography), sanded with very fine P180 grit paper and covered with black paint. The blade has a NACA0018 profile with a span of $s = 15$ cm and a chord of $c = 6$ cm, yielding a chord-to-diameter ratio of $c/D = 0.2$. The turbine blade is fully submersed and its top is located at $h_0 = 12$ cm below the water level. This yields a Froude number $\mathrm{Fr} = \frac{\mathrm{U}_\infty}{\sqrt{g h_0}} \in [0.26 - 0.65]$ for our tested range of tip-speed ratio $\lambda \in [1.2 - 3]$.

The turbine's compact geometry allowed for a blockage ratio of 12.5 %, based on the ratio of the turbine's swept area, given by the blade's span times the rotor diameter, and the water channel's cross-section. The blade is held by a cantilevered shaft such that there is no central strut interference with the flow. At low tip-speed ratios, the effective blockage is closer to 2.5 %, which is the blockage ratio calculated based on the ratio of the blade area, given by the blade's chord times its span, to the cross-sectional area. Additionally, a 2.5 chord length distance to the water channel's side walls is also respected at all times. Based on these observations, we consider the blockage and confinement effects small, and we did not apply any blockage correction to the force measurements (Parker et al., 2017; Ross & Polagye, 2020). This assumption is supported by a numerical simulation of a single-bladed wind turbine with a 32 % blockage ratio conducted by Simão Ferreira et al. (2008).

The turbine model is driven by a NEMA 34 stepper motor with a 0.05° resolution for the angular position. The rotational frequency was kept constant at 0.89 Hz to maintain a constant chord-based Reynolds number of $\mathrm{Re}_c = (\rho \omega R c)/\mu = 50\,000$, where ρ is the density and μ the dynamic viscosity of water. To investigate the role of the tip-speed ratio in the occurrence of dynamic stall, we systematically vary the water channel's incoming flow velocity from 0.14 m/s to 0.70 m/s to obtain tip-speed ratios ranging from 1.2 to 6.

2. Load measurements

The blade shaft was instrumentalised with twenty strain gauges forming five full Wheatstone bridge channels to record unsteady aerodynamic loads acting on the blade. The strain gauges are powered and their output signal is amplified using an instrumentation amplifier with precision voltage reference placed on a printed circuit board that is mounted directly on the rotor arm. The load cell was calibrated in situ using a fully orthogonal calibration rig and undergoing 1350 independent loading conditions. A calibration matrix was obtained by performing a linear regression on the calibration measurements. This matrix contained the 95 % confidence interval of the coefficients allowing an estimation of the uncertainty related to numerous factors, including response linearity, hysteresis, repeatability, and measurement error. The uncertainty was found to be below 5 % for the shear force and pitching moment components. A full description of the calibration procedure that includes the loading conditions, calibration matrix calculation, and error estimation can be found in the appendix of our previous work (Le Fouest & Mulleners, 2022).

For each experiment, the wind turbine model starts at rest with the blade facing the incoming flow. The turbine blade is then accelerated to its prescribed rotational speed. After reaching the target rotational speed, we wait for five full turbine rotations before starting the load recordings. Aerodynamic forces acting on the turbine blade are recorded at 1000 Hz for 100 full turbine rotations, then the blade is brought to rest. The forces presented in this paper are the two shear forces applied at the blade's mid-span in the radial F_R and azimuthal F_θ direction, and the pitching moment about the blade's quarter-chord $M_{1/4}$. The total force applied to the blade is computed by combining the two shear forces: $F_\mathrm{tot} = \sqrt{F_\mathrm{R}^2 + F_\theta^2}$. All force coefficients are non-dimensionalised by the blade chord c, the blade span s, and the blade velocity $\mathrm{U_b} = \omega R$ such that:

$$C_{\mathrm{tot/R}/\theta} = \frac{F_{\mathrm{tot/R}/\theta}}{0.5\rho \mathrm{U_b}^2 sc} \quad .$$

The subscripts tot, R, or θ refer to the total force, the radial, or the tangential force component. The centripetal force resulting from the turbine's rotation was experimentally measured by operating the wind turbine in air. The added drag from the two splitter plates was measured and offset for all investigated tip-speed ratios by operating the wind turbine without the blade, where the two splitter plates were held by a small cylinder. The influence of the centripetal force and the splitter plate are subtracted from the raw measurement data to isolate and compare the aerodynamic forces acting on the turbine blade. A more detailed description of the measurement and modelling of the non-aerodynamic forces is included in the appendix of our previous work (Le Fouest & Mulleners, 2022). The presented force data was filtered using a second-order low-pass filter with the cut-off frequency at 30 Hz. This frequency is multiple times larger than the pitching frequency and approximately 50 times larger than the expected post-stall vortex shedding frequency based on a chord-based Strouhal number of 0.2 (Roshko, 1961).

3. Particle image velocimetry

High-speed particle image velocimetry (PIV) was used to measure the flow field around the wind turbine blade. A dual oscillator diode-pumped ND:YLF laser (λ = 527 nm) with a maximum pulse energy of 30 mJ and a beam splitter were used to create two laser sheets from opposite sides of the channel. The light sheets were oriented horizontally at mid-span of the turbine blade. A high-speed camera with a sensor size of 1024 px × 1024 px (Photron Fastcam SA-X2) and a spinning mirror apparatus were installed below the channel to capture the flow around the blade. The spinning mirror apparatus comprises two rotating and one stationary mirror, all oriented with a 45° angle with respect to the horizontal plane. The two moving mirrors rotate about the same axis of rotation and at the same frequency as the wind turbine. One of the mirrors is placed at the same radius as the model blade, such

that it keeps the blade in the field of view of the camera at all times. The spinning mirror apparatus allows us to measure the velocity field around the blade with a higher spatial resolution and without scarifying the temporal resolution. The field of view is 2.5 c × 2.5 c centred around the blade. The acquisition frequency is 1000 Hz. The images were processed following standard procedures using a multi-grid algorithm (Raffel et al., 2007). The final window size was 48 px × 48 px with an overlap of 75 %. This yields a grid spacing or physical resolution of 1.7 mm = 0.029c. A window overlap above 50 % was selected to minimise spatial averaging of the velocity gradients by the interrogation window following Richard et al. (2006); Kindler et al. (2011). The out-of-plane vorticity component was calculated from the in-plane velocity components using a central difference scheme. Outliers were identified and removed based on a vorticity threshold and median filter. A missing-vector rate of 2 % was estimated accross the different measurements series.

Due to the unsteady effective flow condition experienced by the blade throughout each rotation, the particle displacement between consecutive camera images varies greatly. To have sufficient particles displacement between correlated images and similar relative displacements errors at all azimuthal rotor positions, we have used a variable image skip. We have skipped a different number of particle images depending on the expected flow velocities at a given location and experimental conditions. The number of images skipped between the correlated images was determined based on the expected particle displacement assuming that the flow velocity away from the blade matches the effective flow velocity. When the blade is at an azimuthal location where the expected effective velocity is low, more images are skipped and the time delay between the correlated images is increased. When the blade is at an azimuthal location where the expected effective velocity is high, no or fewer images are skipped and the time delay between the correlated images is decreased. At all positions, we aimed for a minimal partical displacement of 12 px when the flow moves with the nominal effective velocity.

4. Phase-averaging

Load measurements were obtained and phase-averaged over 100 wind turbine revolutions for all tip-speed ratio cases. Phase-averaging involves splitting the phase space into 540 bins that cover 0.67° without overlap. For each bin, we calculate the mean performance value and its standard deviation. This method allows us to visualise the mean performance of the turbine blade at 540 phase positions and the corresponding cycle-to-cycle variations of the performance. The number of bins was selected to be large enough such that sufficient data points lie in each bin and small enough to reduce the smoothening of the data. The acquired data and bin size yielded converged average and first-order statistical metrics of the unsteady aerodynamic loads experienced by the blade.

In addition to the load measurements, we conducted time-resolved velcoity field measurements using PIV for the tip-speed ratios $\lambda \in \{1.2, 1.5, 2, 2.5, 3\}$. For every tip-speed-ratio, we collected a total of 21 838 instantaneous particle images at an acquisition rate of 1000 Hz. The images have been pairwisely correlated using variable image gaps to obtain instantaneous velocity fields. These instantaneous velocity fields were then divided into 200 bins that each cover 1.8° without overlap. The same azimuthal resolution is used for all tip-speed-ratios. The azimuthal resolution for the velocity field phase-averaging is smaller than for the load phase-averaging. The velocity fields were recorded for 21 turbine rotations. The load data was recorded for 100 rotations. The rotational velocity of the turbine was 0.89 Hz for all tip-speed-ratios as the tip-speed-ratio was altered by changing the incoming flow velocity.

Proper orthogonal decoposition is applied on the resulting phase-averaged flow fields. This operation drastically decreases the computational cost, which scales with the number of snapshots squared.

5. Fourth POD mode

The first three spatial POD modes and the corresponding time coefficients for tip-speed ratios $\lambda = 1.2, 1.5, 2.0, 2.5$ and 3.0 are included in the main manuscript. They have been used to identify the dynamic stall development stages.

The fourth POD mode, which plays a more prominent role than the third mode for higher tip-speed ratios where stall is less prominent, did not provide additional information for the identification of the stall stages. It is shown in figure 1 for reference.

The fourth spatial mode represents the second leading-edge vortex that forms in the downwind half. The time coefficients indicating the contribution of the fourth POD mode reach higher values for the higher tip-speed ratios ($\lambda = 2$, 2.5, and 3) than for the low tip-speed ratio ($\lambda = 1.2$ and 1.5). For low tip-speed ratios, the downwind half is mostly dominated by deep post-stall conditions and fully separated flow, whereas the higher tip-speed ratio cases are generally able to recover and form a second coherent leading-edge vortex, yielding an improved efficiency.

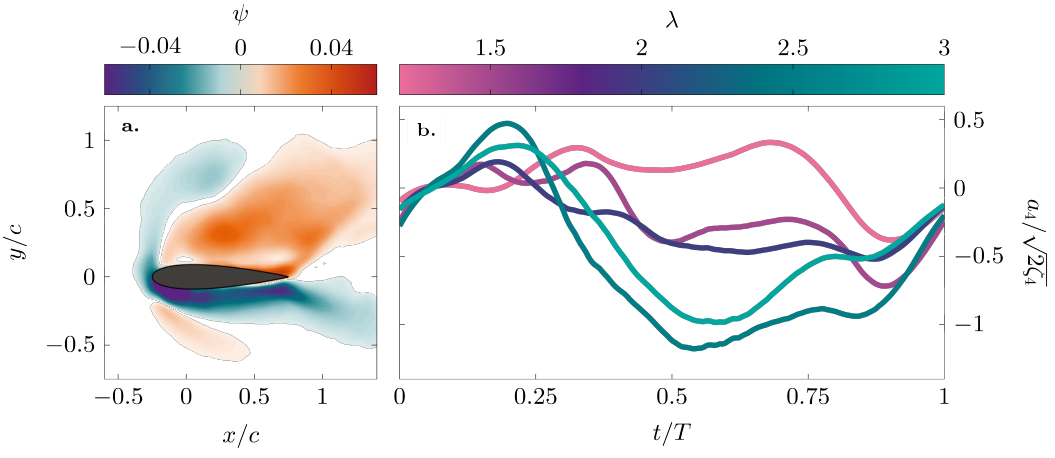

Figure 1. *(a) Fourth spatial POD mode and (b) the evolution of the corresponding time coefficients for tip-speed ratios* $\lambda = 1.2, 1.5, 2.0, 2.5$ *and* 3.0.

6. Aternative viewing angles of the time coefficient parametric curves

The stage detection is based on inflection points in the three dimensional parametric curves. Depending on the orientation of the plot, not all inflection points are clearly visible. Additional views are presented in figure 2.

References

Roshko, A. (1961). Experiments on the flow past a circular cylinder at very high Reynolds number. *Journal of Fluid Mechanics*, *10*(3), 345–356, 1469-7645.

Richard, H., Bosbach, J., Henning, A., Raffel, M., Willert, C., & Wall, B. G. v. d. (2006). 2C and 3C PIV measurements on a rotor in hover condition. In *13th International symposium on applications of laser techniques to fluid mechanics*. Lisbon, Portugal.

Raffel, M., Willert, C. E., Wereley, S. T., & Kompenhans, J. (2007). *Particle Image Velocimetry*. Springer Berlin Heidelberg, Berlin, Heidelberg. ISBN 978-3-540-72307-3.

Simão Ferreira, C., Van Kuik, G., van Bussel, G., & Scarano, F. (2008). Visualization by PIV of dynamic stall on a vertical axis wind turbine. *Experiments in Fluids*, *46*(1), 97–108, 07234864.

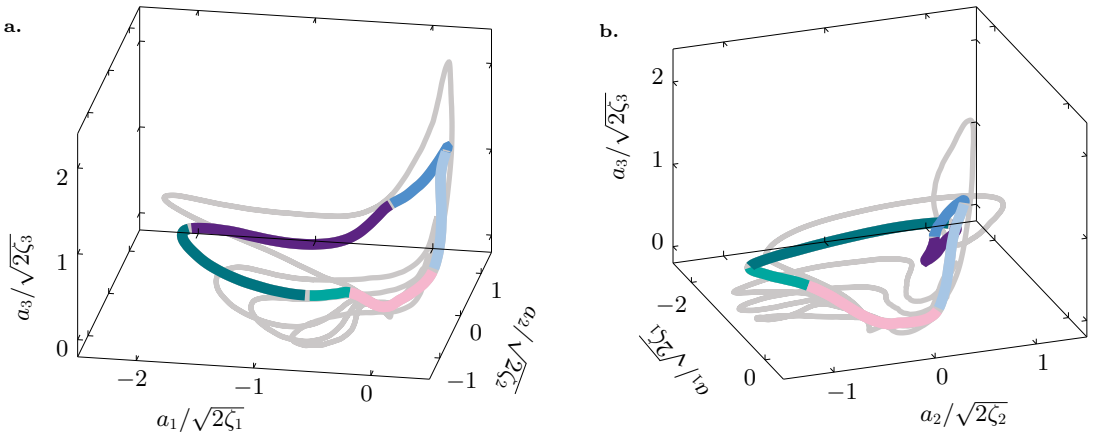

Figure 2. *Time coefficient parametric curve obtained from the stacked vorticity field POD, similar to figure 6a in the manuscript, but under two different orientations. The curve corresponding to tip-speed ratio* $\lambda = 1.5$ *is highlighted.*

Kindler, K., Mulleners, K., Richard, H., van der Wall, B. G., & Raffel, M. (2011). Aperiodicity in the near field of full-scale rotor blade tip vortices. *Experiments in Fluids*, *50*(6), 1601–1610, 0723-4864, 1432-1114.

Parker, C. M., Araya, D. B., & Leftwich, M. C. (2017). Effect of chord-to-diameter ratio on vertical-axis wind turbine wake development. *Experiments in Fluids*, *58*(12), 1–11, 07234864.

Ross, H. & Polagye, B. (2020). An experimental assessment of analytical blockage corrections for turbines. *Renewable Energy*, *152*, 1328–1341, 18790682.

Le Fouest, S. & Mulleners, K. (2022). The dynamic stall dilemma for vertical-axis wind turbines. *Renewable Energy*, *198*, 505–520, 0960-1481.